Journal of Power Sources 183 (2008) 651–659

Contents lists available at ScienceDirect

Journal of Power Sources

journal homepage: www.elsevier.com/locate/jpowsour

Oxidation and electrical behavior of nickel/lanthanum chromite-coated stainless steel interconnects

Nima Shaigan*, Douglas G. Ivey, Weixing Chen

Department of Chemical and Materials Engineering, University of Alberta, Edmonton, Alberta, Canada T6G 2G6

ARTICLE INFO

Article history:
Received 11 April 2008
Received in revised form 7 May 2008
Accepted 8 May 2008
Available online 16 May 2008

Keywords:
Solid oxide fuel cells
Composite electrodeposition
Interconnect
Ferritic stainless steel

ABSTRACT

Solving the contact resistance and cathode-chromium-poisoning problems associated with the application of ferritic stainless steel as solid oxide fuel cell interconnects is the objective of numerous current research efforts. In this work, the application of electrodeposited Ni/$LaCrO_3$ composites for AISI 430 stainless steel as protective/conductive coatings has been studied, with emphasis on the oxidation behavior, scale structure and electronic conductivity of these coatings. The oxidation tests were performed at 800 °C in air for up to 2040 h. The results showed that the scale is a double layer consisting of a particle filled chromia-rich subscale and an outer Ni/Fe-rich spinel together with NiO. The addition of $LaCrO_3$ particles greatly enhances the high-temperature oxidation resistance of Ni-coated ferritic stainless steel. Cavities, which form beneath the scale for uncoated steels as a result of cation outward diffusion, reduce the actual contact area between the scale and the alloy resulting in a high area specific resistance (ASR) as well as scale spallation. Excellent, stable ASR (0.005 Ω cm^2 after 400 h) was achieved with the application of Ni/$LaCrO_3$ coatings.

1. Introduction

Recently, reduction of the operating temperature of solid oxide fuel cells (SOFCs) to less than 800 °C has led to the replacement of problematic ceramic interconnects (lanthanum chromites), which are costly and require high temperatures (~1000 °C) to achieve an acceptable conductivity, with high-temperature alloys [1]. Among the high-temperature oxidation resistant alloys, ferritic stainless steels have been found to be the one of the most practical materials for SOFC interconnect applications due to their low cost, excellent formability to complex shapes, good thermal and electrical conductivity and thermal expansion coefficient compatibility with other cell components [1,2]. Unavoidable high-temperature oxidation and the formation of chromia on ferritic stainless steels during service, particularly on the cathode side, present significant challenges. The most serious problems caused by chromia formation include chromium poisoning of the cathode material (e.g., lanthanum strontium magnetite) [3–7] and an unacceptably high electronic contact resistance, both of which degrade cell performance in relatively short periods of service [2].

Various alloy/surface modifications, as well as the application of protective/conductive coatings, have been developed and studied to eliminate or reduce the aforementioned problems [8–10]. More recent research, however, has concentrated on the application of protective/conductive spinel coatings, such as $(Mn,Co)_3O_4$ [10–16], $(Cu,Mn)_3O_4$ [15,16] and Co_3O_4 [17]. Numerous techniques have been developed to apply spinel coatings to ferritic stainless steels. These include slurry coatings [10–13], anodic electrodeposition [14] and cathodic electrodeposition of particular metals or alloys, followed by annealing/oxidation in air [15–17]. The latter method has been attracting attention due to its low cost, ease of fabrication, the formation of a dense spinel structure and, most notably, good adhesion between the electrodeposited coating and substrate.

During high-temperature annealing/oxidation processes, performed deliberately to produce spinels, a portion of the electrodeposited metal diffuses into the substrate and leaves the alloy dilute in chromium. This can result in a below-threshold Cr concentration (normally ~12 wt%) in the alloy substrate surface. A critical Cr concentration is required for formation of a protective chromia subscale. Consequently, without formation of such a protective chromia subscale, oxidation resistance will not be achieved. Non-uniform (nodular) oxidation may occur where the non-protective, thick chromia subscale breaks down chemically or mechanically.

In an effort to increase the conductivity of oxidized AISI 430 steel interconnects, an electrodeposited composite coating of $LaCrO_3$ particles in a Ni matrix has been developed by the authors [18].

* Corresponding author. Tel.: +1 7804928849.
E-mail address: nshaigan@ualberta.ca (N. Shaigan).

0378-7753/$ – see front matter © 2008 Elsevier B.V. All rights reserved.
doi:10.1016/j.jpowsour.2008.05.024

Table 1
Chemical composition of AISI 430 stainless steel

Element	Concentration (wt%)
Fe	Balance
C	0.12 max
Cr	16–18
Mn	1 max
Si	1 max
S	0.03 max
P	0.04 max

From the preliminary short-term oxidation tests presented in [18], it has been shown that Ni/$LaCrO_3$-coated AISI 430 steels form a slowly growing, spallation free and double layer oxide scale at 800 °C in air. The inner scale is a chromia-rich layer containing $LaCrO_3$ particles and the outer scale is a layer of Ni/Fe-rich spinel containing Mn and Cr as well as NiO. This oxide structure is expected to exhibit and maintain an acceptable electrical conductivity. Moreover, superior oxidation resistance was observed for Ni/$LaCrO_3$-coated steels in comparison with pure Ni-coated samples.

The objective of the current work is to study and characterize the long-term (up to 2040 h at 800 °C) oxidation behavior and the oxide scale electrical properties for Ni/$LaCrO_3$-coated AISI 430 steels.

2. Experimental methods

Coupons of AISI 430 stainless steel, measuring 20 mm × 10 mm × 1 mm were used as substrates. The composition of AISI 430 stainless steel is listed in Table 1. Specimens were cleaned, activated and electrodeposited with Ni/$LaCrO_3$ from a Watts nickel-plating bath containing 20 g L^{-1} of suspended $LaCrO_3$ particles with an average size of ~1 μm. The deposits were ~7 μm thick and contained ~30 vol.% $LaCrO_3$. For the purpose of comparison, identical samples were also electroplated with pure Ni to a thickness of ~7 μm. The detailed deposition procedure is described in our previous work [18]. Oxidation tests were performed for specimens in static air at 800 °C for up to 2040 h.

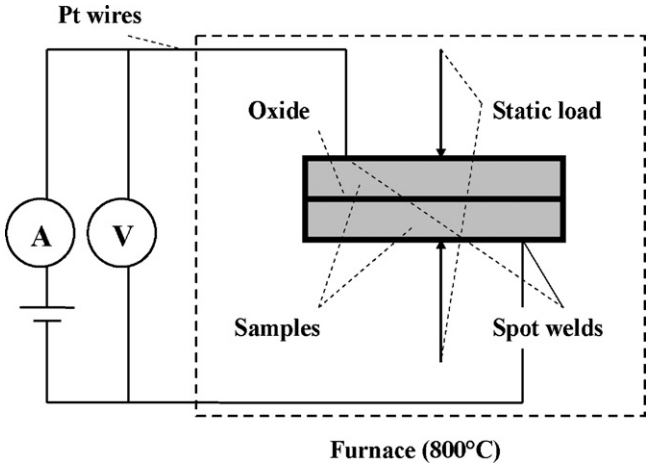

Fig. 1. Experimental set-up for measuring the electrical contact resistance of oxide scales.

Conventional grinding and polishing methods were used for cross-sectional sample preparation. A Hitachi H2700 scanning electron microscope (SEM), equipped with a Princeton Gamma-Tech (Prism IG) ultra thin window (UTW) energy dispersive X-ray (EDX) spectrometer was used for imaging and chemical analysis. A Rigaku Geigerflex 2173 rotating anode system was employed for the purpose of glancing angle ($\theta = 2°$) X-ray diffraction (XRD) analysis and phase identification of oxidized specimens. The X-ray penetration depth for this angle was about 10 μm. Due to spatial resolution limitations, associated with EDX analysis, depth profiling for oxidized (170 and 2040 h) Ni/$LaCrO_3$-coated specimens was performed by means of secondary ion mass spectrometry (SIMS). The instrument employed for this purpose was an Ion-ToF SIMS IV. Specimens were sputtered with Cs^+ ions at 1 keV and 250 nA. The sputtering area was 200 μm × 200 μm. Ga^+ ion sputtering at 15 keV over an area of 34 μm × 34 μm was used for analysis. A JEOL Auger scanning microprobe (JAMP 9500F) was used for surface analysis and elemental mapping of oxidized Ni/$LaCrO_3$-coated AISI 430 steels. A Sartorius (CP225D) high precision balance was used to measure sample

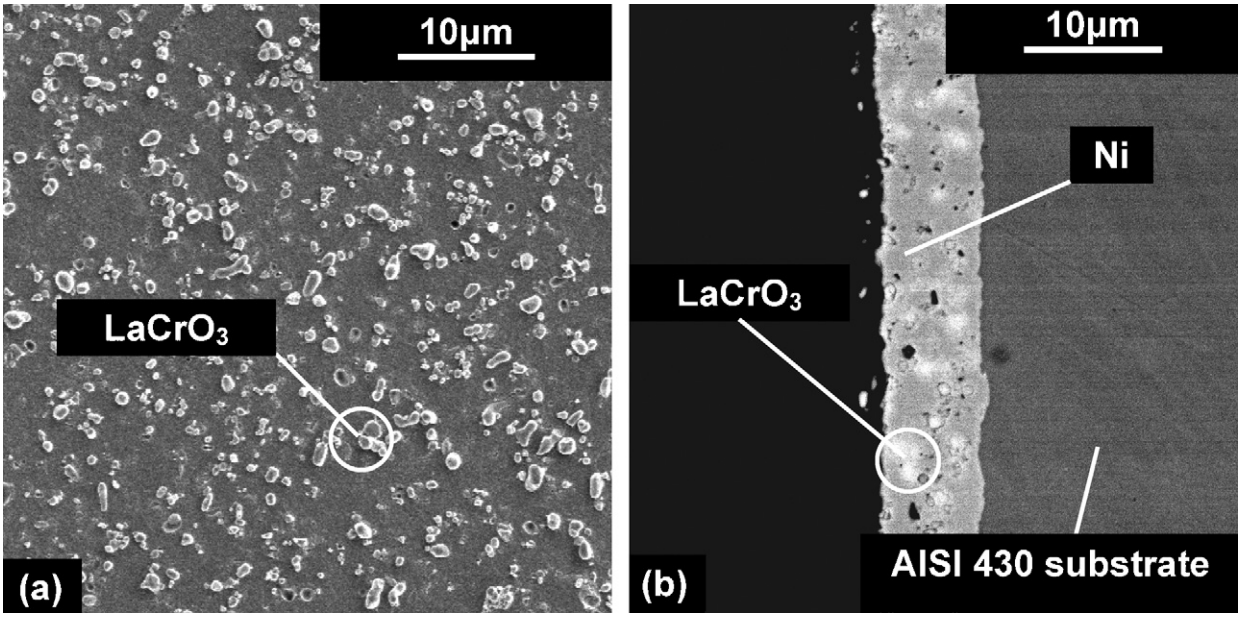

Fig. 2. SEM images of an as-deposited Ni/$LaCrO_3$-coated AISI 430 steel. (a) Plan view secondary electron (SE) image and (b) cross-sectional backscattered electron (BSE) image.

Table 2
Compositions (at%) determined by EDX point analysis for different regions shown in Fig. 3

Regions (points)	Fig. 3a and b (170 h)					Fig. 3c and d (2040 h)				
	Fe	Ni	Cr	Mn	Si	Fe	Ni	Cr	Mn	Si
(1)	12	84	3	1	0	15	78	3	4	0
(2)	57	40	1	2	0	45	44	3	8	0
(3)	16	27	50	2	5	13	7	73	7	0
(4)	64	21	11	2	2	78	7	13	1	1

weight gain after oxidation. For this purpose, three identical samples were used. After various time intervals, the same specimens were taken out of the furnace, air-cooled and weighed.

In order to measure the area specific resistance (ASR) of the oxidized samples, the set-up shown in Fig. 1 was employed. Platinum wires were spot welded to one side of two identical non-oxidized samples to provide electrical connections. To avoid alloy-to-alloy adhesion and erroneous results, platinum wire welded coupons were pre-oxidized for 24 h at 800 °C. No conductive paste, which may affect the oxidation mechanism, was applied between the two samples. To prevent contact being lost between samples, a static load of 9.8 N was applied to the samples. A constant current density of 300 mA cm^{-2} was applied and the voltage was recorded every 120 s. An electrochemical measurement instrument, Gamry Series G 300, was employed for this purpose. The data were used to calculate the resistance according to Ohm's law and the ASR as a product of the resistance and surface area. In order to measure the resistance contribution from the junctions, wires and the alloy, two platinum wires were spot welded to the sides of a single AISI 430 coupon and the resulting resistance was subtracted from the original test results. All the above-mentioned tests, including ASR and other oxidation tests, were run at 800 °C in an electric box furnace and static air.

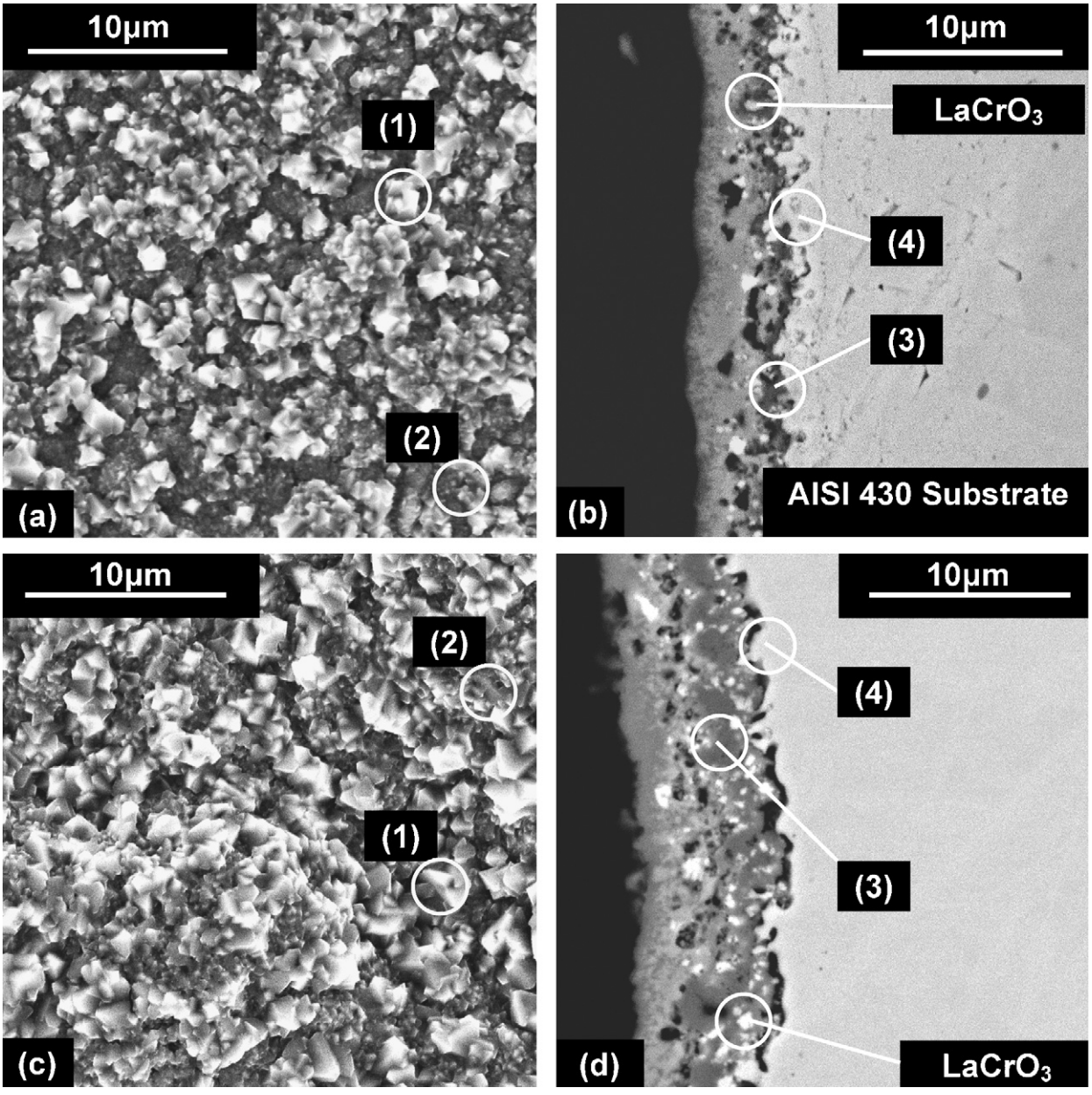

Fig. 3. SEM images of oxidized Ni/$LaCrO_3$-coated AISI 430 stainless steels: (a) and (b) after 170 h; (c) and (d) after 2040 h of oxidation in air at 800 °C. (a) and (c) are plan view SE images; (b) and (d) are cross-sectional BSE images.

3. Results and discussion

3.1. As-deposited coating structure

Fig. 2 shows a secondary electron (SE) plan view SEM image (Fig. 2a) and a backscattered electron (BSE) cross-sectional SEM image (Fig. 2b) of an as-deposited Ni/$LaCrO_3$-coated sample. The samples were prepared using the optimal conditions described in Ref. [18]. The coatings contain ~30 vol.% of embedded $LaCrO_3$ particles in Ni. Embedded particles, uniformly distributed in a level Ni matrix, are seen in both images of Fig. 2. Good adhesion between the coating and the substrate, as well as a uniform distribution of particles throughout the coating thickness are seen in Fig. 2b. Pull-outs of particles are visible in Fig. 2b; these arise from ultrasonic cleaning, grinding and polishing.

3.2. Scale characterization

SEM plan view and cross-sectional images of Ni/$LaCrO_3$-coated specimens, oxidized for 170 and 2040 h at 800 °C in air, are shown in Fig. 3. The compositions of the numbered regions on the images were determined by EDX analysis and are listed in Table 2. Oxygen levels are not shown in the table.

Fig. 3a and c shows that the oxide surfaces consist of some large oxide particles (region (1) in Fig. 3a and c) embedded in a fine-grained matrix (region (2) in Fig. 3a and c). EDX analysis (Table 2) shows that the coarse particles are rich in Ni (>70 at%), while the matrix grains of the coating are rich in both Fe and Ni. Both regions contain small amounts of Mn and Cr (<1 at%). No cracks and/or spalled areas were observed on the surface, even though the samples were air-cooled from 800 °C to room temperature.

From Fig. 3b and d, it is evident that the oxide scales consist of two distinguishable layers. The brighter outer layer, which is also seen in the plan view images (Fig. 3a and c), shows different regions of dark and light contrast in the BSE images (Fig. 3b and d). The regions with higher concentrations of Ni appear lighter. This outer scale retains its thickness over the oxidation period as seen in Fig. 3b and d. According to the EDX analysis (Table 2), the concentrations of both Mn and Cr in this layer increase slightly with increasing oxidation time. The Mn concentration increases more noticeably in region (2). The Cr concentration does not exceed 3 at% in the outer scale. This indicates that Cr migration to the scale surface and consequently Cr volatization has been inhibited. The apparent porosity seen in the cross-sectional images (Fig. 3b and d) are particle pull-outs, resulting from polishing and ultrasonic cleaning.

The inner scale (region (3) in Fig. 3b and d) is rich in Cr, and also contains Mn, Fe and Ni. This layer grows as the oxidation time is increased. The $LaCrO_3$ particles are distributed throughout this Cr-rich subscale. An adherent, but uneven alloy–scale boundary is seen for the specimen oxidized for 170 h (Fig. 3b). Porosity at the alloy–scale interface, however, is seen for the specimen oxidized for 2040 h (Fig. 3d).

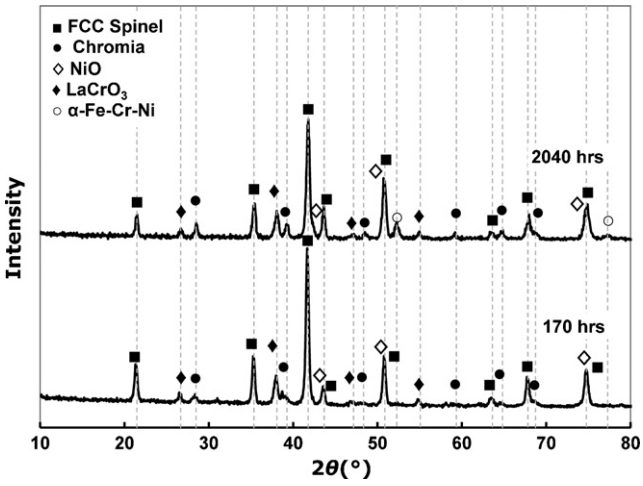

Fig. 4. XRD patterns for Ni/$LaCrO_3$-coated AISI 430 stainless specimens oxidized for 170 and 2040 h.

The presence of 21 at% Ni in the substrate surface region (region (4)) for the specimen oxidized for 170 h shows that a portion of Ni diffuses into substrate during initial oxidation. After long-term oxidation, the Ni concentration in the same region drops to 7 at%. The decrease in the Ni content is not due to oxidation, since the thickness of the outer scale, containing Ni, does not increase substantially. Therefore, during high-temperature oxidation, Ni diffuses into the substrate and is replaced with Fe and Cr diffusing out from the substrate towards the alloy–scale interface.

The phases that form in the Ni/$LaCrO_3$-coated specimens during oxidation for 170 and 2040 h were identified by means of glancing angle X-ray diffraction with the aid of EDX microanalysis. The XRD patterns from the scales are shown in Fig. 4. The identified phases for the sample oxidized for 170 h include FCC spinel, rhombohedral chromia (with Fe, Ni and Mn), cubic NiO and perovskite-type $LaCrO_3$. There may be peaks from the FCC Fe–Ni–Cr substrate surface region present in the patterns, but they overlap with FCC spinel and NiO peaks, making identification inconclusive. Also, some peaks for the FCC spinel and NiO phases overlap, but EDX analysis confirms their presence. In addition to the phases identified for the sample oxidized for 170 h, two BCC substrate peaks at $2\theta = 52.34°$ ($d_{110} = 0.2028$ nm) and $2\theta = 77.18°$ ($d_{200} = 0.143$ nm) appear in the pattern obtained from the specimen oxidized for 2040 h. Since Ni is a well know austenite stabilizer in stainless

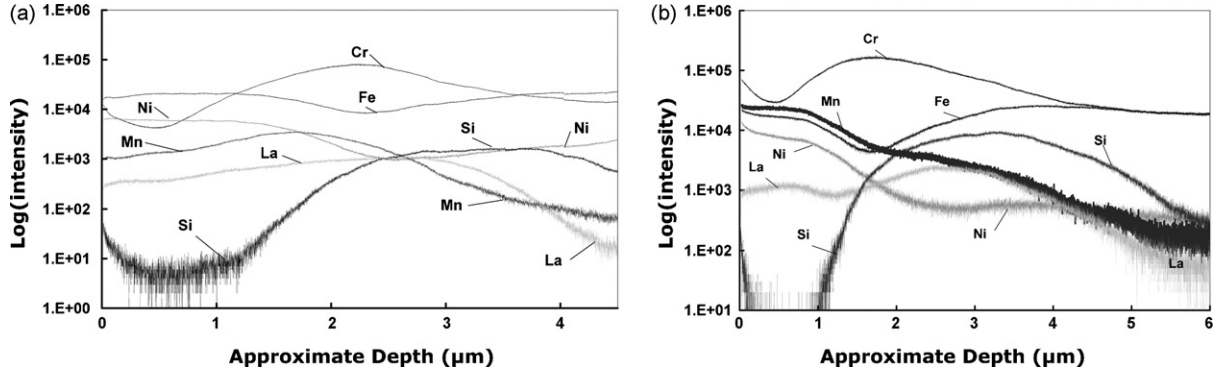

Fig. 5. SIMS depth profiles for oxidized Ni/$LaCrO_3$-coated AISI 430 stainless specimens for (a) 170 h and (b) 2040 h of oxidation.

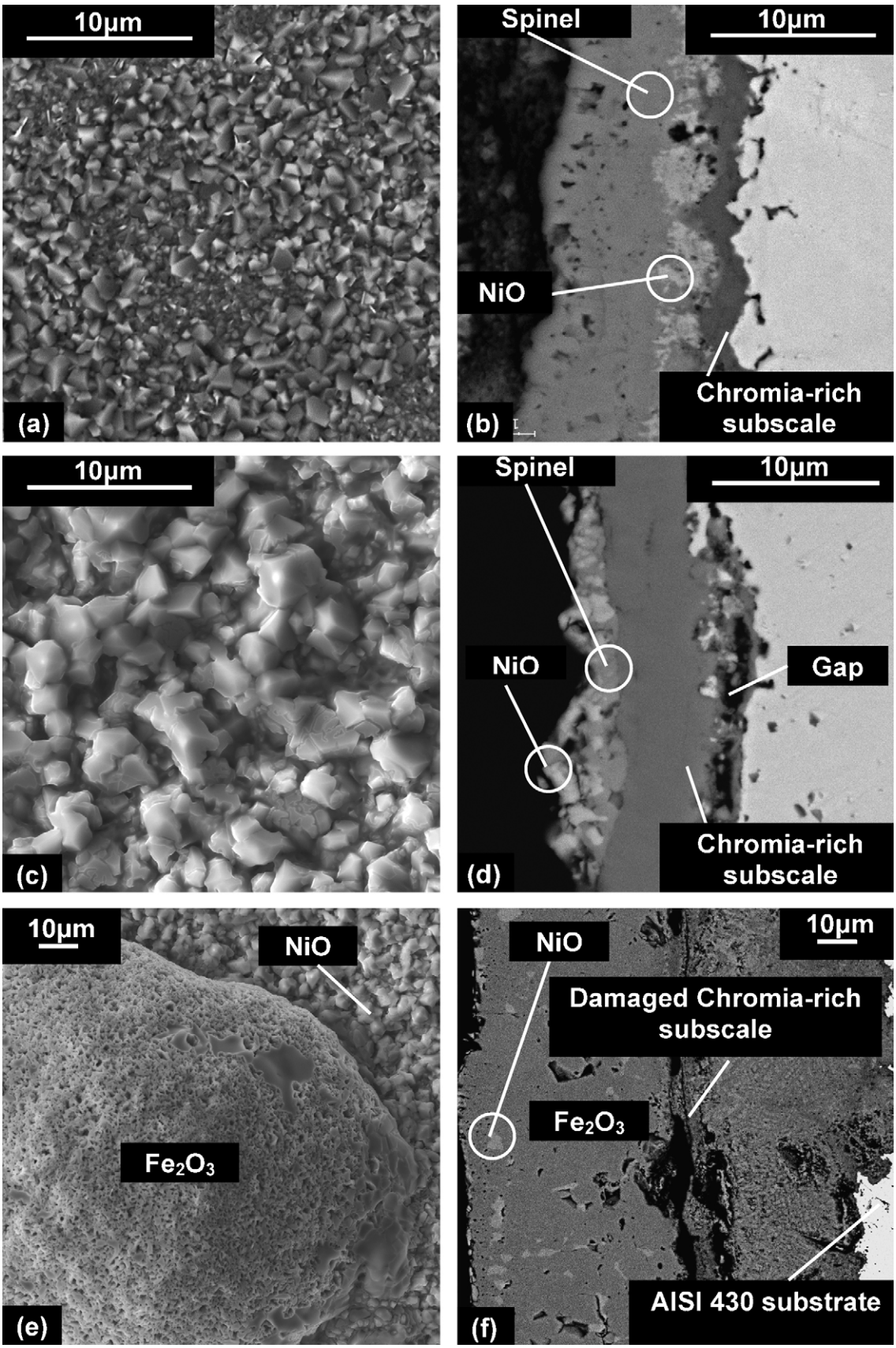

Fig. 6. SEM images for oxidized Ni-coated AISI 430 stainless steels: (a) and (b) after 170 h; (c)–(f) after 2040 h of oxidation in air at 800 °C. (e) and (f) show oxide nodules; (a), (c) and (e) are plan view SE images; (b), (d) and (f) are cross-sectional BSE images.

steels, an FCC to BCC phase transformation was likely in the surface region of the substrate, adjacent to the scale, due to a drop in the Ni concentration from 21 at% (170 h of oxidation) to 7 at% or less after further oxidation (2040 h).

The peaks identified as chromia-rich are more intense for the specimen oxidized for 2040 h than those for 170 h of oxidation. This indicates that more of the chromia-rich phase has formed for samples oxidized for 2040 h than for samples oxidized for 170 h. This is consistent with the cross-sectional images in Fig. 3b and d.

SIMS depth profiles for Ni/$LaCrO_3$-coated specimens oxidized for 170 and 2040 h are shown in Fig. 5. Both Cr profiles show a maximum in the chromia-rich subscale. The Cr intensity increase in the spinel/NiO layer, near the surface, is seen in both profiles. This may be due to Cr solubility in the spinel phase. EDX analysis results from cross-sectional images do not show more than 3 at% Cr in the spinel/NiO layer. The Fe and Ni profiles exhibit a decrease through the chromia-rich layer followed by an increase in the outer scale. The Mn profile shows a high concentration of Mn in the outer oxide layer, which corresponds to the spinel layer. Manganese is able to easily diffuse through the chromia-rich subscale into the outer scale. Comparison between Fig. 5a and b shows that the Mn content in the spinel phase increases with oxidation time. EDX results (Table 2) also confirm that the amount of Mn in the spinel phase has increased from 2 to 8 at% (region (2) in Fig. 3a and c) with increasing oxidation time from 170 to 2040 h. Silicon segregation (likely as SiO_2) is evident at the alloy-scale interface beneath the chromia-rich subscale. This segregation is more noticeable in Fig. 5b for the sample oxidized for 2040 h. Lanthanum appears in the entire scale depth with a higher concentration in the chromia-rich scale where most of particles are located. The presence of La on the surface, where there are no $LaCrO_3$ particles in the SEM images (Fig. 3a and c), indicates that La ions diffuse from the particles present throughout the scale.

In summary, the thermally grown oxide scale forming on the surface of Ni/$LaCrO_3$-coated AISI 430 stainless steels is a double layer consisting of a slowly growing, particle filled chromia-rich subscale, containing some Fe, Ni and Mn, and a complex Ni–Fe–Mn–Cr spinel/NiO outer scale which does not grow significantly with oxidation time. The 3 at% Cr (determined by EDX) in the outer scale (Table 2) also indicates that Cr migration from the chromia-rich subscale has been effectively limited by the outer scale. Segregation of Si (likely as SiO_2) at alloy/scale interface is clearly seen, although the layer does not appear to be continuous (Fig. 3b and d). The porosity at the alloy/scale interface for the sample oxidized for 2040 h (Fig. 3d) may be due to the formation of this discontinuous silica layer. Silica is not miscible with chromia [19,20] and the adhesion between the two oxides is poor. This may result in detachment of chromia from the underlying silica network, which is adherent to the substrate, and the formation of porosity at the alloy/scale interface.

3.3. *Effect of $LaCrO_3$ particles on oxidation behavior*

In order to determine the effect of $LaCrO_3$ particles on the oxidation behavior of Ni/$LaCrO_3$-coated samples, identical substrates were plated with pure Ni to the same thickness (~7 μm) and oxidized under the same conditions as the Ni/$LaCrO_3$-coated samples. SEM plan view and cross-sectional images of these samples are shown in Fig. 6. A thicker scale, in comparison with that grown on the Ni/$LaCrO_3$-coated specimens, forms on the Ni-coated samples. A wide gap is also visible between the substrate and scale in Fig. 6d. It is clear from comparing Fig. 6a and c that the outer oxide particles for the Ni-coated samples have grown significantly larger from 170 to 2040 h of oxidation, relative to what was seen for the Ni/$LaCrO_3$-coated steels shown in Fig. 3a and c. For these samples, only a small change in oxide particle size occurred. Large, isolated nodules of oxide start to form and grow on the surface of Ni-coated samples after oxidation times longer than 600 h. Examples are shown in Fig. 6e and f for a Ni-coated specimen oxidized for 2040 h. XRD analysis of the Ni-coated samples (not shown here) indicated that the nodules were Fe_2O_3; chromia, spinel and NiO were also identified.

According to EDX analysis, the concentration of Cr in the substrate surface does not exceed ~9 at%, which is below the critical concentration of Cr (11 at%) needed to form a protective chromia layer. The drop in Cr concentration at the surface of substrate is due to inward diffusion of a portion of the non-oxidized Ni, which also occurs for the Ni/$LaCrO_3$-coated samples. In addition, there is rapid outward diffusion of Cr, contributing to formation of a thick chromia-rich subscale. For Ni/$LaCrO_3$-coated samples oxidized for 2040 h, the concentration of Cr at the surface of the substrate is 11 at% (Table 2, region (4)). This indicates that for the composite coating, less Cr contributes to the formation of the chromia-rich layer and that a more protective, less permeable chromia-rich layer forms in the presence of the $LaCrO_3$ particles. No damage to the chromia-rich subscale, with the corresponding formation of oxide nodules, was observed even after 2040 h of oxidation for Ni coatings with $LaCrO_3$.

Fig. 7 shows the specific weight gains for cyclically oxidized Ni/$LaCrO_3$-coated, Ni-coated and uncoated AISI 430 stainless steels. Ni/$LaCrO_3$-coated and uncoated steels show a similar weight gain trend, except for the initial stage when Ni oxidizes faster than the uncoated steel. Ni-coated samples, however, exhibit notably faster oxidation rates in comparison with both Ni/$LaCrO_3$-coated and uncoated steels. Exponential oxidation kinetics is seen after 600 h when Fe oxide nodules start to appear and grow. From the SEM images (Figs. 3 and 6) and weight gain results (Fig. 7), it is evident that Ni/$LaCrO_3$-coated steels exhibit superior oxidation resistance, in terms of scale growth rate and formation of a protective scale, over Ni-coated samples.

The marked improvement in the oxidation resistance is attributed to the presence of $LaCrO_3$ particles, which is the only difference between the Ni/$LaCrO_3$-coated and Ni-coated samples. Lanthanum, present in the dispersed particles, is considered to be a reactive element (RE) which can greatly improve the oxidation resistance of high-temperature alloys [21].

Auger electron spectrometry (AES) was performed for Ni/$LaCrO_3$-coated specimens oxidized for 2040 h. In addition to Ni, Fe, Mn, Cr and O, trace amounts of La and S were detected on the oxide surface. Sulfur is present as an impurity in the steel (to a

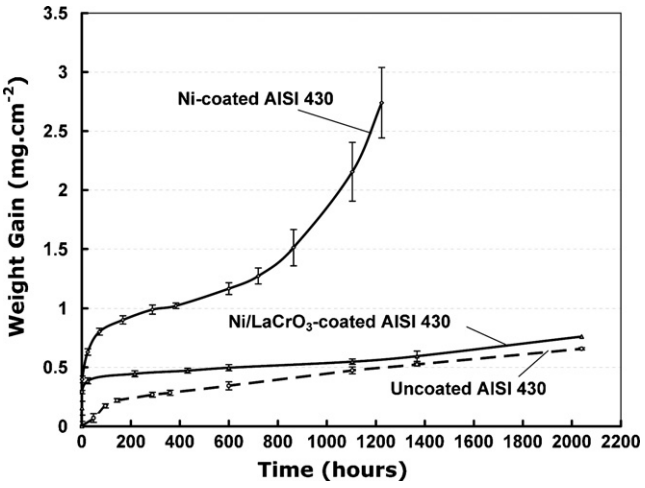

Fig. 7. Specific weight gains for oxidized Ni/$LaCrO_3$-coated, Ni-coated and uncoated AISI 430 stainless steels as a function of oxidation time.

maximum of 0.03 at%). Also, the Ni-plating solution may introduce trace amounts of co-deposited sulfur to the coating, although a saccharin-free bath was used. Fig. 8 depicts an SE image (Fig. 8a) and the corresponding Auger electron maps for La (Fig. 8b) and S (Fig. 8c). Regions appearing brighter on the maps correspond to higher concentrations of the elements in question, i.e., La and S. Regions that show up darker have negligible concentrations of the elements. Lanthanum shows a higher concentration along the crystal edges and grain boundaries. Sulfur is detected in grain boundary junctions, indicated by the circled regions. Where sulfur is concentrated, La is also present with a higher concentration than for the rest of surface. This indicates that sulfur is associated with lanthanum.

The "sulfur effect" theory proposed by Lees [22] explains the reactive element and oxide dispersion influence on oxidation resistance enhancement for high-temperature alloys. According to this theory, the impurity S has two detrimental effects on oxidation resistance. The first effect is that S tends to segregate to oxide grain boundaries and enhance cation migration, while it has almost no effect on oxygen transport. The second effect is that S segregates to the metal–oxide interface and reduces scale adhesion dramatically, causing buckling of the scale. According to the "sulfur effect" hypothesis, finely dispersed oxide particles (both reactive oxides and other stable oxides) in the alloy adsorb a large portion of impurity sulfur and eliminate its detrimental effects.

According to Pint's "dynamic-segregation" theory [23], reactive elements have a strong affinity for oxygen. Due to this driving force, reactive elements tend to migrate to the scale surface where the activity of oxygen is higher than that in the scale and the substrate. Reactive ions diffuse through oxide grain boundaries, which are rapid diffusion pathways. Because of their large ionic radii, reactive ions tend to segregate to oxide grain boundaries during their

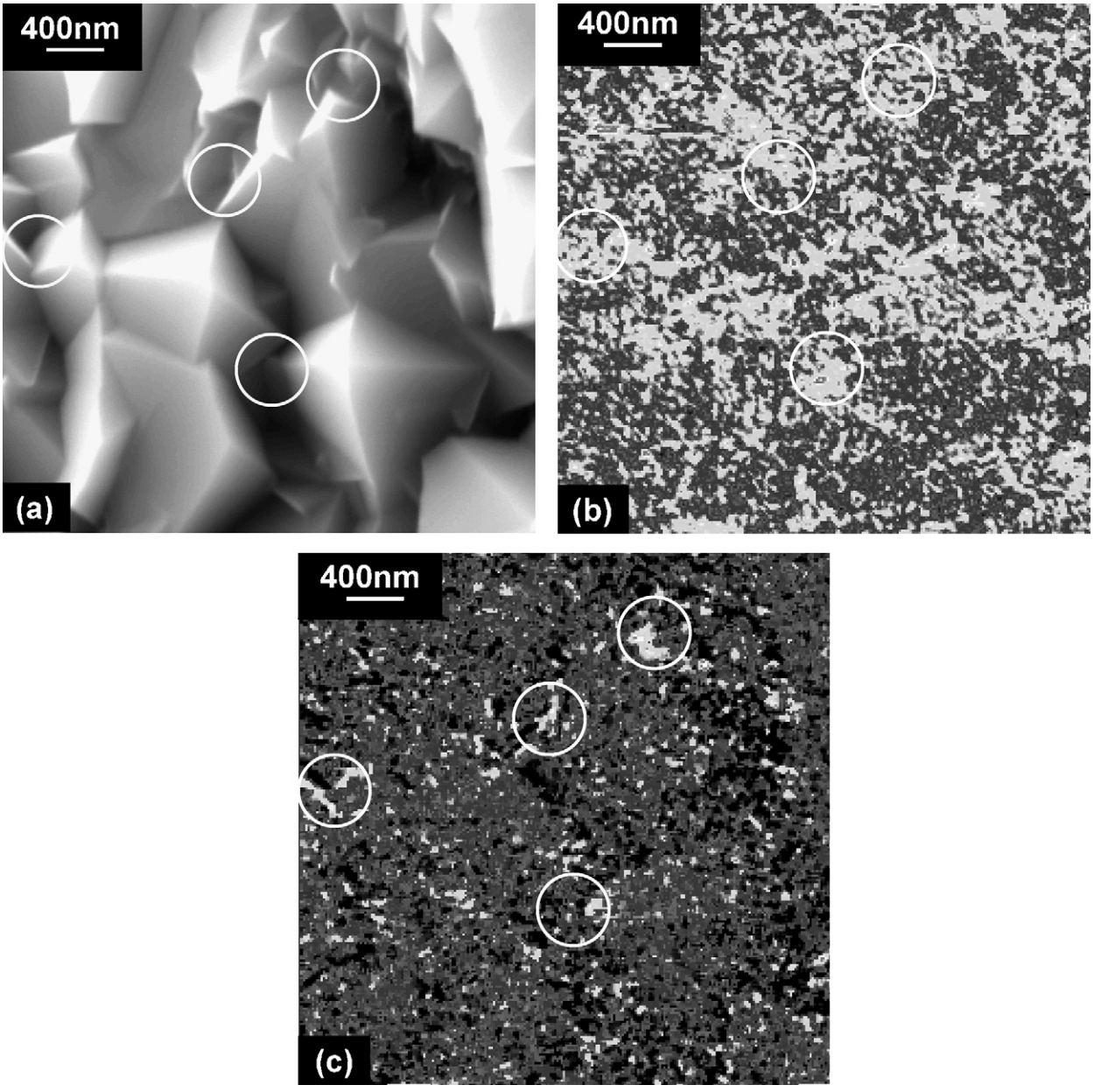

Fig. 8. SE image (a) and corresponding La (b) and S (c) Auger electron maps for Ni/$LaCrO_3$-coated AISI 430 steel, oxidized for 2040 h in air at 800 °C.

migration. Such segregation of reactive ions at the grain boundaries blocks paths for cation outward diffusion. This reduces the scale growth rate and grain size and changes the oxide formation mechanism from being predominantly cation outward diffusion to oxygen anion inward diffusion.

Since S was detected along with La on the oxide surface, it is evident that relatively large (~1 μm) dispersed $LaCrO_3$ particles are not able to adsorb the S impurities to a great extent. This is consistent with Wright et al. [24], who suggest that coarse oxide dispersions do not provide a large enough metal–oxide interface area to effectively adsorb S.

Sulfur facilitates the cation outward migration [22] while La reduces cation diffusion rates due to its blocking of the rapid diffusion paths [23]. Sulfur, in this work, is always associated with La in the oxide scale. Therefore, cation diffusion cannot be promoted by S when La blocks the cation diffusion paths. It is proposed that La supplied by $LaCrO_3$ particles reduces the deleterious effect of S on oxidation resistance. Also, by blocking the diffusion paths, the addition of La changes the oxidation mechanism from a predominantly outward cation diffusion process to and inward anion diffusion process resulting in better adhesion of the scale.

3.4. Area specific resistance (ASR)

A major objective of this work is to enhance the high-temperature electronic conductivity of AISI 430 stainless steel interconnects.

Fig. 9 shows the ASR of uncoated and Ni/$LaCrO_3$-coated AISI 430 stainless steels at 800 °C, as a function of time. The ASR profile for uncoated AISI 430 shows a parabolic trend which approaches 0.035 Ω cm^2 after 250 h. For the Ni/$LaCrO_3$-coated AISI 430, the ASR value does not exceed 0.005 Ω cm^2 after 400 h. This value is considerably smaller than that for the uncoated AISI 430 steel.

The oxide scale that has formed on uncoated AISI 430, after 170 h of oxidation at 800 °C in air, is ~1 μm thick and consists of a chromia-rich subscale and a $(Mn,Cr)_3O_4$ spinel outer scale. A thin, continuous layer of silica forms beneath the chromia-rich subscale. The oxide scale grows to a thickness of ~2 μm after 2040 h of oxidation. Fig. 10 shows a region beneath some buckled scale on an AISI 430 specimen, oxidized for 170 h in air at 800 °C. Underneath the scale are several ~20 μm wide or larger cavities. These cavities lead to the formation of gaps between the scale and the substrate. Cavity formation is attributed to outward diffusion of cations (Cr, Si and Mn ions) from the grain boundaries of the alloy surface during oxidation. This hypothesis was confirmed by Auger electron spectra taken from the cavities and substrate surface underneath the scale (Fig. 11). Fig. 11a shows a spectrum from the surface of a cavity. Only oxide forming/diffusing elements, Cr, Mn and Si, were detected on the surface. The spectrum from the substrate surface in the cavity (Fig. 11b) shows the presence of bulk steel components, Fe and Cr. Oxygen and C are also present and are considered as common contaminants.

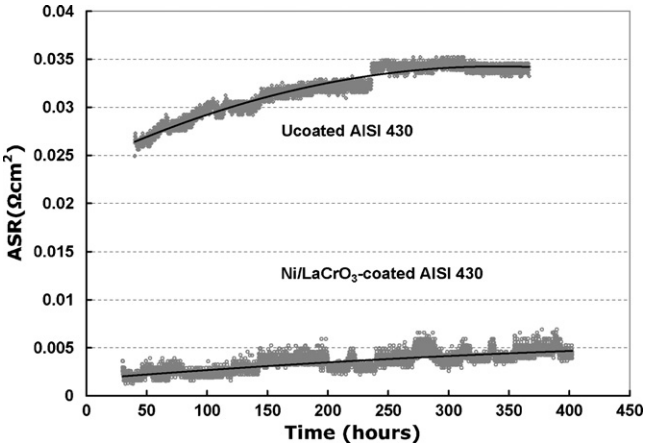

Fig. 9. Measured ASR values for Ni/$LaCrO_3$-coated and uncoated AISI 430 stainless steel at 800 °C in air as a function of time.

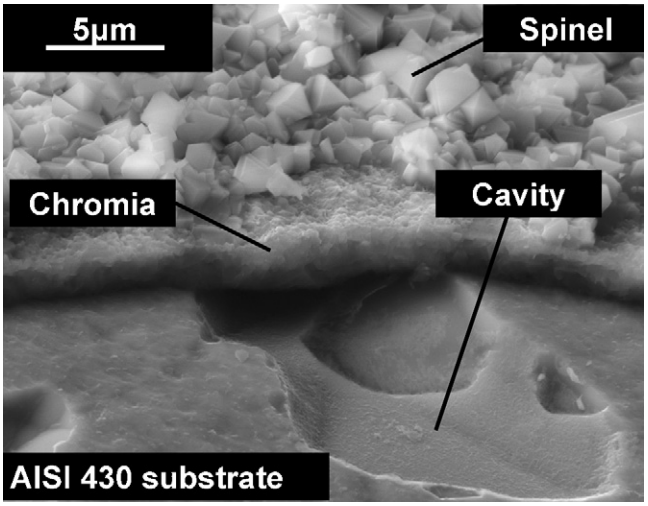

Fig. 10. SEM SE image of a spalled area on an AISI 430 stainless steel oxidized for 170 h in air at 800 °C. The specimen was tilted 40°.

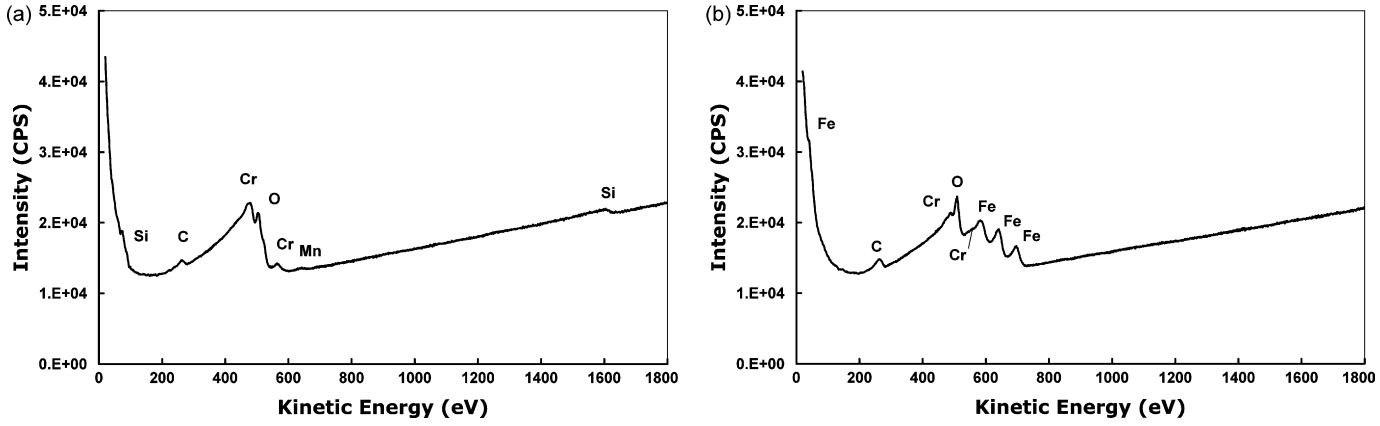

Fig. 11. Auger electron spectra of (a) cavity and (b) substrate surface shown in Fig. 10.

The formation of these cavities reduces the actual contact surface area between the alloy and scale. This leads to a higher ASR value, which is the product of the resistance and the nominal contact surface area of the scale and alloy. It is clear that changing the oxidation mechanism from outward cation diffusion to inward oxygen anion diffusion eliminates or reduces the formation of these cavities, which decrease the actual contact area between the scale and substrate resulting in large ASR values. No spallation or formation of cavities is observed for $Ni/LaCrO_3$-coated steels.

In addition to elimination or reduction of the diffusion cavities beneath the scale, the significantly reduced ASR by application of $Ni/LaCrO_3$ coatings can be attributed to the presence of conductive $LaCrO_3$ particles in the chromia-rich subscale and good scale adhesion. However, the electronic conductivity of the chromia scale itself is not possible (or, at least, not easy) to calculate or measure, due to the resistance contributions from the imperfect alloy-scale interface where an insulating SiO_2 layer is also detected (Fig. 5).

4. Conclusions

1. The oxide scale, which forms on the surface of $Ni/LaCrO_3$-coated AISI 430 stainless steels, consists of a subscale of $LaCrO_3$ particle filled and adherent chromia and an outer scale composed of a Ni/Fe-rich complex spinel (containing Mn and Cr) as well as NiO.
2. No buckling of the scale, which occurs for uncoated AISI 430 steels, was observed for oxidized $Ni/LaCrO_3$-coated AISI 430 stainless steels even during air cooling from 800 °C.
3. Oxidation resistance has been greatly improved by the addition of $LaCrO_3$ particles to Ni coatings, due in part to the reduction by La of the deleterious effects of the impurity S in the steel.
4. Cavities form as the result of grain boundary outward migration of cations during oxidation of uncoated AISI 430 stainless steels. The formation of these cavities reduces the actual contact area between the scale and alloy, resulting in high ASR values.
5. A stable low ASR value ($0.005\ \Omega\ cm^2$ after 400 h at 800 °C) was obtained for $Ni/LaCrO_3$ coatings.

Acknowledgements

The authors wish to thank the Natural Sciences and Engineering Research Council (NSERC) of Canada and Versa Power Systems for providing research funding.

References

[1] W.Z. Zhu, S.C. Deevi, Materials Research Bulletin 38 (2003) 957–972.
[2] W.Z. Zhu, S.C. Deevi, Materials Science and Engineering A 348 (2003) 227–243.
[3] S.P. Jiang, J.P. Zhang, L. Apateanu, K. Foger, Journal of the Electrochemical Society 147 (11) (2000) 4013–4022.
[4] W.J. Quadakkers, J. Piron-Abellan, V. Shemet, L. Singheiser, Materials at High Temperatures 20 (2) (2003) 115–127.
[5] C. Gindorf, L. Singheiser, K. Hilpert, Journal of Physics and Chemistry of Solids 66 (2005) 384–387.
[6] J.W. Fergus, International Journal of Hydrogen Energy 32 (16) (2007) 3664–3671.
[7] S.P. Jiang, Journal of European Ceramic Society 22 (3) (2002) 361–371.
[8] K. Huang, P.Y. Hou, J.B. Goodenough, Materials Research Bulletin 36 (2001) 81–95.
[9] W. Qu, J. Li, D.G. Ivey, J.M. Hill, Journal of Power Sources 157 (1) (2006) 335–350.
[10] X. Chen, P.Y. Hou, C.P. Jacobson, S.J. Visko, L.C. De Jonghe, Solid State Ionics 176 (2005) 425–433.
[11] Z. Yang, G. Xia, S.P. Simner, J.W. Stevenson, Journal of the Electrochemical Society 152 (9) (2005) 1896–1901.
[12] Z. Yang, G. Xia, X. Li, J.W. Stevenson, International Journal of Hydrogen Energy 32 (2007) 3648–3654.
[13] Z. Yang, G. Xia, J.W. Stevenson, Electrochemical and Solid-State Letters 8 (3) (2005) A168–A170.
[14] W. Wei, W. Chen, D.G. Ivey, Chemistry of Materials 19 (2007) 2816–2822.
[15] M.R. Bateni, P. Wei, X. Deng, A. Petric, Surface & Coating Technology 201 (2007) 4677–4684.
[16] P. Wei, X. Deng, M.R. Bateni, A. Petric, Corrosion 63 (6) (2007) 529–536.
[17] X. Deng, P. Wei, M.R. Bateni, A. Petric, Journal of Power Sources 160 (2006) 1225–1229.
[18] N. Shaigan, D.G. Ivey, W. Chen, Journal of the Electrochemical Society 155 (4) (2008) D278–D284.
[19] M.L. K'eith, in: E.M. Levin, et al. (Eds.), Phase Diagrams for Ceramists, The American Ceramic Society, 1964, Fig. 332.
[20] Z. Yang, International Materials Reviews 53 (1) (2008) 39–54.
[21] D.P. Whittle, J. Stringer, Philosophical Transactions of the Royal Society of London, Series A: Mathematical and Physical Sciences 295 (1980) 309–329.
[22] D.G. Lees, Oxidation of Metals 27 (1–2) (1987) 75–81.
[23] B.A. Pint, Oxidation of Metals 45 (1–2) (1996) 1–37.
[24] I.G. Wright, B.A. Wilcox, R.I. Jaffee, Oxidation of Metals 9 (3) (1975) 275–305.